

MOX–Report No. 16/2013

## **Metal Artifact Reduction in Computed Tomography Images by Variational Inpainting Methods**

FAGGIANO, E. ; LORENZI, T. ; QUARTERONI, A.

MOX, Dipartimento di Matematica “F. Brioschi”  
Politecnico di Milano, Via Bonardi 9 - 20133 Milano (Italy)

[mox@mate.polimi.it](mailto:mox@mate.polimi.it)

<http://mox.polimi.it>



# Metal Artifact Reduction in Computed Tomography Images by Variational Inpainting Methods \*

E. Faggiano<sup>1,2</sup>, T. Lorenzi<sup>3</sup>  
and A. Quarteroni<sup>1,4</sup>

April 8, 2013

<sup>1</sup> MOX– Modellistica e Calcolo Scientifico  
Dipartimento di Matematica “F. Brioschi”  
Politecnico di Milano, Milano, Italy  
`elena.faggiano@mail.polimi.it`, `alfio.quarteroni@polimi.it`

<sup>2</sup> Laboratory of Biological Structure Mechanics(LaBs)  
Department of Chemistry, Material and Chemical Engineering  
Politecnico di Milano, Milan, Italy

<sup>3</sup> Department of Mathematical Sciences  
Politecnico di Torino, Torino, Italy  
`tommaso.lorenzi@polito.it`

<sup>4</sup> SB MATHICSE CMCS,  
EPFL de Lausanne, Lausanne, Switzerland.  
`alfio.quarteroni@epfl.ch`

---

\*This work has been partially supported by the ERC Advanced Grant N.227058 MATH-CARD and by the FIRB project - RBID08PP3J.

**Keywords:** Metal Artifact Reduction, Computed Tomography, Image Inpainting, Variational and PDE Methods

### Abstract

Permanent metallic implants such as dental fillings, hip prostheses and cardiac devices generate streaks-like artifacts in computed tomography images. In this paper, two methods based on partial differential equations (PDEs), the Cahn-Hilliard equation and the TV- $H^{-1}$  inpainting equation, are proposed to reduce metal artifacts. Although already profitably employed in other branches of image processing, these two fourth-order variational methods have never been used to perform metal artifact reduction. A systematic evaluation of the performances of the two methods is carried out. Comparisons are made with the results obtained with classical linear interpolation and two other PDE-based approaches using, respectively, the Fourier heat equation and a nonlinear version of the heat equation relying on total variation flow. Visual inspection of both synthetic and real computed tomography images, as well as computation of similarity indexes, suggest that the Cahn-Hilliard method behaves comparably with more classical approaches, whereas the TV- $H^{-1}$  method outperforms the others as it provides best image restoration, highest similarity indexes and for being the only one able to recover hidden structures, a task of primary importance in the medical field.

## 1 Introduction

Metal artifacts represent a serious problem in X-ray Computerized Tomography (CT) as they are commonly observed in images of patients with permanent metallic implants (*e.g.* dental fillings, hip prostheses, cardiac devices etc.). They originate from beam hardening, which is due to high X-ray attenuation of the metallic parts and allows only a limited number of photons to reach the CT detectors. The radiation intensities collected by CT detectors are organized, in function of projection angle and detector position, in the so-called sinogram matrix. Metal artifacts lead to inconsistent sinogram projections, which alter the image reconstruction process and result into dark streaks surrounded by bright streaks that can seriously degrade image quality, especially in the presence of high atomic number metals (*e.g.* iron or platinum)[1].

During the past three decades, various approaches which are generally referred to as Metal Artifact Reduction (MAR) techniques have been proposed for reducing artifacts caused by metallic implants. They can be *prima facie* classified as iterative reconstruction methods and interpolation-based methods.

Iterative methods operate directly on the original raw sinogram data and compensate for the missing projections through modified versions of classical iterative reconstruction algorithms. They are divided into two main groups: algebraic techniques (*e.g.* algebraic reconstruction and simultaneous iterative reconstruc-

tion [2, 3]) and statistical techniques (*e.g.* maximum likelihood-expectation maximization algorithms [4, 5]). The need of original raw sinogram data, which are often unavailable, and the high computational costs represent the major drawbacks of these techniques.

On the other hand, interpolation-based methods aim at identifying the corrupted parts of the sinogram and replacing them using information coming from the uncorrupted neighboring projections. Usually, these methods are less computationally expensive than the iterative ones and can be implemented starting from the reconstructed image. As a result, they do not require original raw projection data. They typically consist in four steps: segmentation of metal regions in the native image, forward projection of the image and forward projection of the metal, sinogram restoration, reconstruction of the final image via Filtered Back Projection (FBP). The strategies used to perform the sinogram restoration step include, among others, linear interpolation (LI) [6, 7, 8], cubic interpolation [9], spline interpolation [10], wavelet based interpolation [11] and techniques involving either a variational principle, through a minimization process, or a (non necessarily variational) partial differential equation (PDE) [12, 13].

The latter techniques rely on the idea that the missing parts of an image can be filled using information diffused from the nearby areas through a suitable PDE. Using the Fourier’s Heat Equation (HE) is the simplest way to diffuse information. However, due to its regularitazion property, this equation cannot preserve discontinuous image features. In order to address this shortcoming, suitable nonlinear versions of the heat equation have been designed, as the ones relying on Total Variation (TV) flow, where the diffusivity constant depends upon the size of the image gradient, so that diffusion near edges is namely reduced [14]. Although achieving clear improvements over the heat equation, these second-order PDEs still have disadvantages, for instance, they do not perform well on edges spanning large gaps, and this has motivated the use of higher order PDEs for image inpainting. Among fourth-order PDEs, Chan, Shen and Kang [15] proposed in 2003 a new variational inpainting method based on the Euler’s Elastica (EE) that allows for isophotes connection across large distances. Bertozzi, Esedoglu and Gillette [16] introduced in 2007 a new fourth-order method relying on the Chan-Hilliard (CH) equation, which shares the good properties as the EE method and, in addition, can be solved by fast computational techniques [17]. Bertozzi, Burger, He and Schönlieb in 2009 proposed the TV- $H^{-1}$  method as a possible generalization of the CH method, conceived for high contrast or binary images, to gray-value images [18, 19]. The same fast computational technique developed for the CH applies to the TV- $H^{-1}$  method as well [20].

Although profitably employed in other branches of image processing, to the best of our knowledge, these two variational methods have never been used to perform sinogram inpainting. In this paper we propose the use of the CH and TV- $H^{-1}$  methods in the context of MAR.

In more detail, we aim at verifying if sinogram inpainting can be effectively performed by these variational approaches. Section II briefly describes variational

image inpainting, in general, and the variational methods under consideration, in particular. Section III summarizes the results obtained on both synthetic data, *i.e.* a phantom image with metal artifacts, and clinical CT images of patients with metallic implants. The performance of these methods, is observed through visual inspection and similarity indexes, and compared with that of LI, HE and TV inpaintings, which are assumed as standard references. In Section IV a critical discussion of the results of this work and some conclusive considerations are drawn.

## 2 Methods

### 2.1 Variational Image Inpainting

From a mathematical standpoint, a 2D image can be identified with a domain  $\Omega \subset \mathbb{R}^2$  (*i.e.* the image domain) and a function  $u^0$  standing for the image intensity distribution over  $\Omega$ . In this framework, the area of the image to be inpainted can be considered as a set  $D \subset \Omega$  (*i.e.* the inpainting domain) and the inpainting problem consists in using the values attained by the  $u^0$  function in  $\Omega \setminus D$  to find a distribution  $u$  that fills properly  $D$ .

The past few years testified, among the others, the spreading of variational methods for image inpainting. We refer to [18] and the references therein for a general literature on the subject. Such methods rely on the idea that the solution  $u$  of the inpainting problem can be identified with the steady solution of an evolution equation propagating  $u^0$  from  $\Omega \setminus D$  into  $D$ .

In more detail, given open and bounded domain  $\Omega$  with Lipschitz boundary  $\partial\Omega$ ,  $u^0(\cdot) \in L^2(\Omega)$  and  $u(t, \cdot) \in BV(\Omega)$  for all  $t \in \mathbb{R}_+$ , solving an image inpainting problem consists in finding the steady state of the following PDE in the form given hereafter, provided with initial condition  $u(t = 0, \cdot) = u^0(\cdot)$  in  $\Omega$  and Neumann boundary condition on  $\partial\Omega$ :

$$\partial_t u(t, x) = \lambda \chi_{\Omega \setminus D}(x)(u^0(x) - u(t, x)) + R(u), \quad (1)$$

where  $(t, x) \in \mathbb{R}_+ \times \Omega$ ,  $\lambda \in \mathbb{R}_+$  is the so-called fidelity parameter and  $\chi_{\Omega \setminus D}(\cdot)$  is the characteristic function of the set  $\Omega \setminus D$ . Equation (1) can be derived as the Euler-Lagrange equation associated to the following variational problem:

$$\min_{u \in BV(\Omega)} \left\{ \lambda \int_{\Omega \setminus D} |u^0 - u|^2 dx + R(u) \right\}, \quad (2)$$

where the first term is the so-called fidelity term, which keeps memory of the original image, while  $R(u)$  is a regularizing spatial differential operator, whose definition characterizes the inpainting method. The order of the inpainting method is identified by the order of PDE (1).

## 2.2 Fourth Order Variational MAR

The main steps of the strategy here followed to perform MAR are summarized by Figure 1: segmentation of metal parts in the original image by means of a threshold method; subtraction of the metal parts from the original image; forward projection of the image free from the metal parts into the Radon space to obtain the subtracted sinogram; processing of the subtracted sinogram; image reconstruction from the corrected sinogram through FBP; reinsertion of the metallic parts into the reconstructed image to obtain the final corrected image. The novelty of our approach consists in using two fourth order variational in-

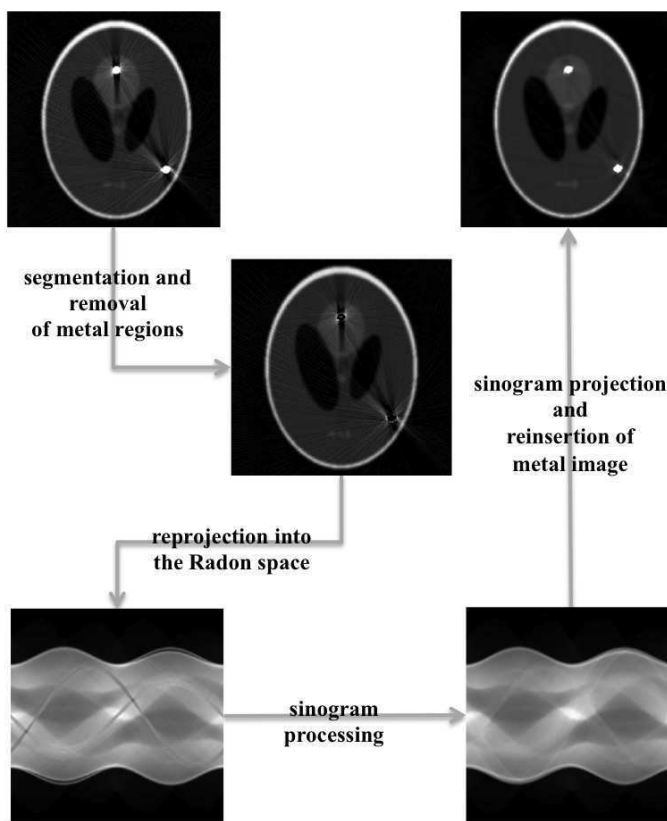


Figure 1: Flowchart of the strategy followed to perform MAR.

painting methods (*i.e.* CH and TV- $H^{-1}$ ) to perform sinogram processing. Using the same notations of the previous subsection, the subtracted sinogram identifies the image domain  $\Omega$  and the projection values define the image intensity distribution  $u^0$ . The area to be inpainted  $D \subset \Omega$  consists in the corrupted projections corresponding to metal parts. The inpainting problem at hand translates into finding a distribution  $u$  of the projection values that fills the corrupted area evolving the distribution  $u^0$  of the uncorrupted projection values through (1)

with:

$$R(u) := \Delta \left( -\varepsilon \Delta u + \frac{1}{\varepsilon} W'(u) \right) \quad (\text{CH}) \quad (3)$$

or

$$R(u) := \Delta (\partial TV(u)) \quad (\text{TV-H}^{-1}). \quad (4)$$

Functional  $\partial TV(u)$  is the subdifferential of functional  $TV(u)$ , which can be approximated as

$$\partial TV(u) \approx \nabla \cdot \left( \frac{\nabla u}{|\nabla u|} \right),$$

while the functional  $W(u)$  is the so-called double-well potential of the Cahn-Hilliard equation. Following [16, 17], we assume

$$W(u) := u^2(u - 1)^2.$$

Plugging one of the definitions above into (1), we obtain a fourth-order PDE. As a result, the ones here considered can be classified as fourth-order variational inpainting methods.

Concerning the numerical scheme adopted to solve the mathematical problem linked to PDE (1) and definition (3), or definition (4), we implement the fast solver proposed by Bertozzi and Schönlieb[20], which is known as convexity splitting.

### 2.3 Performance Evaluation

We apply CH and TV-H<sup>-1</sup> methods on either synthetic data and CT medical images as well.

**Synthetic data** A Shepp-Logan phantom of 256×256 pixels with two metal regions of high attenuation and induced artifacts is generated. Four significant

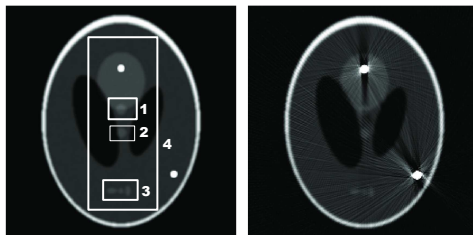


Figure 2: Original phantom (left) and phantom with metal induced artifacts (right). The specific areas used for performance evaluation are highlighted.

regions of the phantom are identified as highlighted by the left panel of Figure 2, which are used for performance evaluation. Region 4 includes metal parts and the majority of the areas affected by metal artifacts. On the other hand,

Regions 1-3 contain little objects that we aim at preserving and enhancing with the MAR procedure. In particular, Region 1 contains an ellipse, partially superimposed on another bigger ellipse, which is made nearly invisible by metal artifacts (see Figure 2, right panel). Region 2 contains another ellipse that is easily distinguishable and segmentable in the original image but not in the image with artifacts. Region 3 contains three distinct ellipses that should be kept distinguishable by the MAR procedure.

Two similarity indexes are computed in Regions 1-4 to evaluate performance: the Peak-Signal-to-Noise Ratio (PSNR) and the Normalized Cross-Correlation Coefficient (NCC). Both these indexes are extensively used in image processing to validate, or evaluate, the results of different methods (*e.g.* in image registration or image inpainting [13]), if a reference exact image is available.

The PSNR is defined as

$$\text{PSNR} := 10 \times \log_{10} \left( \frac{I_{Mref}^2}{\|I_{cor}(\cdot) - I_{ref}(\cdot)\|_{L^2(\Gamma)}^2} \right),$$

where  $I_{Mref} = \max I_{ref}$ , function  $I_{cor}$  stands for the intensity distribution of the artifact corrected image, function  $I_{ref}$  is the intensity distribution of the reference image (*i.e.* the original image without metal artifacts) and  $\Gamma \subset \mathbb{R}^2$  is the related image domain. The greater the PSNR value, the better the performance of the method.

The NCC is defined as:

$$\text{NCC} := \frac{1}{|\Gamma|} \int_{\Gamma} \frac{(I_{cor}(x) - \mu_{cor})(I_{ref}(x) - \mu_{ref})}{\sigma_{cor}\sigma_{ref}} dx,$$

where  $x \in \Gamma$ ,  $\mu_{cor}$  and  $\mu_{ref}$  are, respectively, the average values of the intensity distributions  $I_{cor}$  and  $I_{ref}$ , while  $\sigma_{cor}$  and  $\sigma_{ref}$  are the related standard deviations.

NCC is equal to 1 if the following identity holds:

$$I_{cor}(x) = I_{ref}(x), \quad \forall x \in \Gamma,$$

Both these indexes, although widely used, provide only a global measure of the performance. However, a global good agreement between corrected and reference images could not be sufficient in the medical field. For this reason, we analyze the performance of our method even from a more local perspective. In particular, we segment the ellipses of Regions 2 and 3 both in the image with metal artifacts and in the corrected ones. The obtained segmentations are then compared with those of the reference image making use of the Dice Similarity Coefficient (DSC) [21], a similarity index commonly used in the medical field:

$$\text{DSC} = 2 \frac{|M_{ref} \cap M_{cor}|}{|M_{ref}| + |M_{cor}|}$$

where  $M_{ref}$  and  $M_{cor}$  are the binary masks representing the segmented areas in the reference image and the corrected image, respectively. A DSC value equal to 1 indicates for a perfect matching between the two segmentations.

**Clinical data** Concerning the clinical data, a head-neck CT image of a patient with dental fillings is used to evaluate the performance of the MAR methods. The image is  $512 \times 512$  pixels with pixel size equal to  $0.976 \times 0.976$ . Evaluations are performed through visual inspection of the CT scan and the profile-lines of the attenuation coefficient related to a representative probing line [7, 22, 23].

### 3 Results

Simulations are performed on a 2.27 GHz Intel (R) Core i5 processor, with 3.7 GB RAM and the methods are programmed in MATLAB 64 bit (R2011b, The MathWorks, Natick, MA).

**Synthetic data** At first, we consider the case of the phantom. Simulations related to HE, TV, CH and TV- $H^{-1}$  methods are run for 10000 iterations to allow the related PDEs to reach the steady state. The value of the fidelity parameter  $\lambda$  is set equal to 1 for the HE method, 10 for the TV and TV- $H^{-1}$  methods and 50000 for the CH method.

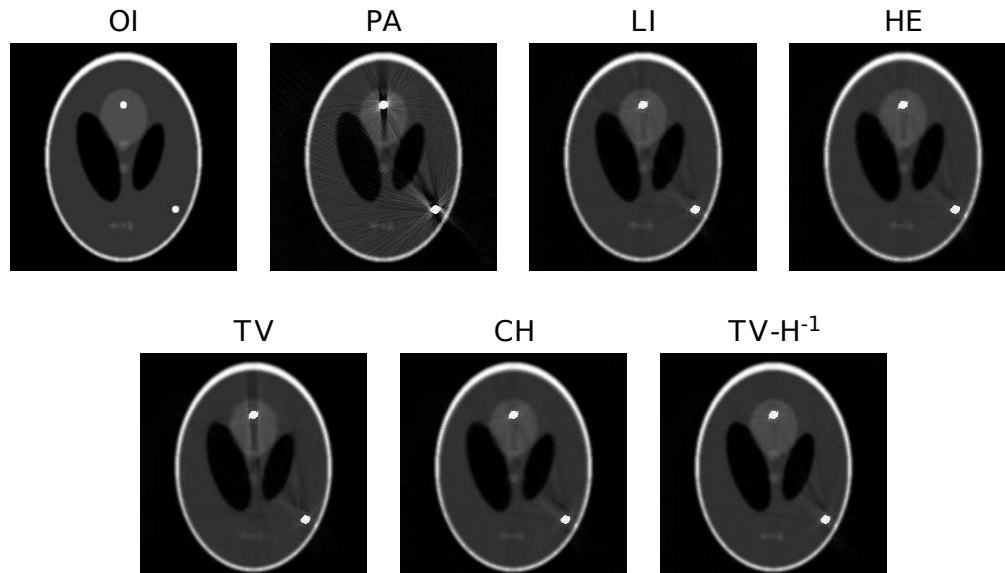


Figure 3: From left to right, from top to bottom, the original image (OI), the image containing metal artifacts (PA) and the corrected images of the MAR procedures relying on the LI, HE, TV, CH and TV- $H^{-1}$  methods.

The obtained results are summarized in Figure 3, where Panel OI refers to the phantom without metal artifacts, Panel PA shows the phantom containing metal artifacts, while Panels from LI to TV- $H^{-1}$  display the corrected images resulting from the MAR procedures relying on the five inpainting methods under consideration. This figure shows how metal artifacts are suppressed to different

extents. The TV- $H^{-1}$  inpainting achieves better visual effects compared to the LI, HE, TV and CH inpaintings. In fact, the results of the TV- $H^{-1}$  method are smoother and characterized by less marked residual artifacts. On the other hand, the other four methods provide a substantial metal artifacts reduction but still maintain more evident residual artifacts in the surrounding of the metallic objects.

Analyzing in more detail each region, the higher performance of the TV- $H^{-1}$  method in preserving and recovering image information can be further appreciated. Going into details, Figure 4 supports the idea that the MAR procedure relying on the TV- $H^{-1}$  method allows to recover hidden structures. In fact, a little ellipse on a non-uniform background is visible in Region 1 of the reference image, while this is totally absent in the image with the metal artifacts. The same ellipse becomes again distinguishable after TV- $H^{-1}$  inpainting of the sinogram, while the other methods here considered are not able to restore such a structure, probably because of its proximity to the metallic object. The worst results are obtained with the TV method. Concerning Region 2 (see Figure 5), all the five analyzed methods are able to recover the shape of the hidden object; the TV method achieves the worst results in this region as well. Finally, focusing on Region 3, not all the methods keep the three ellipses distinguishable. In particular, the LI and TV- $H^{-1}$  methods give better results.

The above considerations are also confirmed by the values attained by the global similarity indexes (see Table 1) in Regions 1-4. In fact, the highest values of the PSNR and the NCC are obtained with the TV- $H^{-1}$  method. It is worth noting that the values related to the LI, HE and CH methods, although smaller than those related to the TV- $H^{-1}$  method, are higher than those of the image with metal artifact. This indicates a good restoration quality. Finally, the lowest values are those obtained using the TV method, which are similar to those of the image with metal artifacts.

Table 1: Similarity indexes evaluated in Regions 1-4 of the image containing metal artifacts (PA), of the images corrected by the MAR procedures relying on the standard reference methods LI, HE, TV and on the fourth-order variational methods CH and TV- $H^{-1}$ .

|              | Region 1 |       | Region 2 |       | Region 3 |       | Region 4 |       |
|--------------|----------|-------|----------|-------|----------|-------|----------|-------|
|              | PSNR     | NCC   | PSNR     | NCC   | PSNR     | NCC   | PSNR     | NCC   |
| PA           | 16.528   | 0.841 | 19.589   | 0.934 | 21.261   | 0.649 | 26.747   | 0.781 |
| LI           | 21.807   | 0.959 | 22.963   | 0.987 | 26.759   | 0.935 | 27.733   | 0.821 |
| HE           | 21.661   | 0.964 | 22.607   | 0.991 | 26.165   | 0.963 | 27.748   | 0.822 |
| TV           | 17.531   | 0.873 | 19.483   | 0.988 | 23.455   | 0.911 | 27.583   | 0.814 |
| CH           | 21.263   | 0.964 | 21.484   | 0.988 | 25.997   | 0.957 | 27.721   | 0.820 |
| TV- $H^{-1}$ | 26.484   | 0.993 | 27.091   | 0.995 | 28.258   | 0.976 | 27.786   | 0.824 |

In order to complete our results assessment, we develop DSC analysis on

Regions 2 and 3. We start by segmenting the ellipses in these regions through a thresholding algorithm to get the binary masks shown by the second rows of Figure 5 and Figure 6, which are then used to compute the DSC indexes summarized by Table 2. Thresholds are chosen independently for each image, in order to optimize the segmentation process.

The obtained results further confirm the conclusions drawn on the basis of visual inspection and global indexes evaluation. As we would expect, the segmentations of the image with metal artifacts are very poor in both regions and the contours of the related ellipses are hardly distinguishable. In particular, a correct segmentation with simple threshold cannot be achieved in Region 2 (see Panel PA in Figure 5). On the other hand, a substantial improvement of the information content is testified by segmentations of the corrected images. In particular, the LI, HE, CH and TV- $H^{-1}$  methods are able to preserve the structures in Region 2 and Region 3 of the original image. In fact, the ellipse in Region 2 is completely recovered (see Figure 5), the three ellipses in Region 3 become well discernible (see Figure 6) and the DSC values are close to 1 (see Table 2), thus demonstrating a good matching between the reference binary masks and the corrected ones. The TV- $H^{-1}$  method features the highest DSC values, while the lowest values are the ones related to the TV method, which namely leads the three ellipses in Region 3 to merge into a single object.

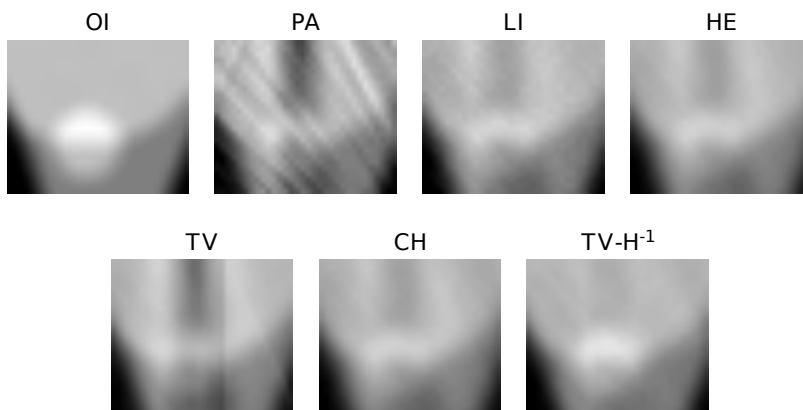


Figure 4: From left to right, from top to bottom, Region 1 of the original image (OI), of the image containing metal artifacts (PA) and of the images corrected by the MAR procedures relying on the LI, HE, TV, CH and TV- $H^{-1}$  methods.

**Clinical data** When considering clinical data, simulations related to HE, TV, CH and TV- $H^{-1}$  methods are run for 10000 iterations to allow the related PDEs to reach the steady state. The value of the fidelity parameter  $\lambda$  is set equal to 1 for both HE and TV- $H^{-1}$  methods, 100 for the TV method and 50000 for the CH method.

The obtained results are summarized in Figure 7, where Panel OI shows the

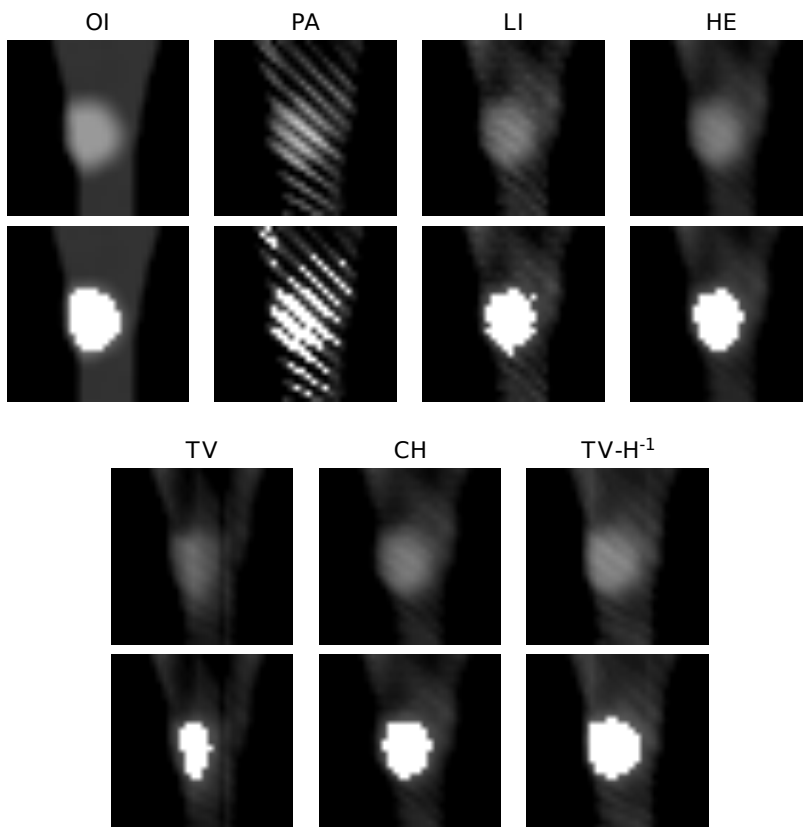


Figure 5: From left to right, from top to bottom, Region 2 (first row) and related segmentation (second row) of the original image (OI), of the image containing metal artifacts (PA) and of the images corrected by the MAR procedures relying on the LI, HE, TV, CH and  $TV-H^{-1}$  methods.

original image with dark, board streaks radiating from the metallic implants. Panels from LI to  $TV-H^{-1}$  illustrate the results obtained with LI, TV, CH and  $TV-H^{-1}$  methods, respectively. In order to further appreciate the modifications introduced by the MAR methods, one representative profile-line of the attenuation coefficient is shown for each image (see white solid lines) in the same figure. Dashed white lines highlight the related probing line, which is selected since it contains metallic parts, soft tissues and metal artifacts in the original image. Metallic implants and bones result into high picks, while dark-band artifacts correspond to concavities with lower attenuation coefficients.

Figure 7 shows how dark streaks are corrected by all the methods, although some residual artifacts still remain in the proximity of the metallic implants. The image resulting from the MAR procedure relying on LI exhibits a more artificial appearance, while bright fictitious artifacts are introduced by the TV method.

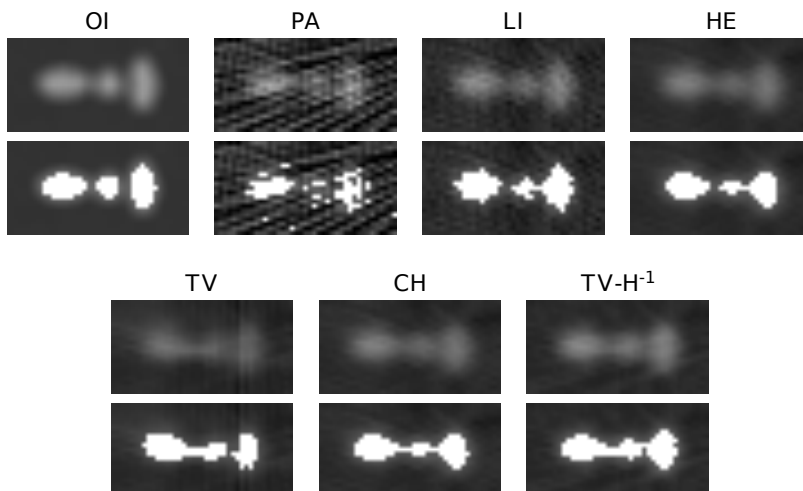


Figure 6: From left to right, from top to bottom, Region 3 (first row) and related segmentation (second row) of the original image (OI), of the image containing metal artifacts (PA) and of the images corrected by the MAR procedures procedures relying on the LI, HE, TV, CH and  $\text{TV-H}^{-1}$  methods.

Looking at the profile-lines, frequent small changes in the attenuation coefficient dominate the profile related to LI, which is the one closer to the profile of the original image with metal artifacts. Such changes are reduced in the image related to the other methods under consideration. In particular, the profile shown in Panel  $\text{TV-H}^{-1}$  is smoother than the others and concavities with lower attenuation coefficients are much less evident. Finally, we would expect the profile-line between the two high picks to be almost flat, since the anatomic conformation suggests a constant attenuation coefficient in the region of the palate. This scenario is partially recovered by the TV method and faithfully reproduced by the  $\text{TV-H}^{-1}$  method. These considerations lead us to conclude that the best results can be obtained with the  $\text{TV-H}^{-1}$  method.

Table 2: DSC index evaluated in Regions 2-3 of the image containing metal artifacts (PA), of the images corrected by the MAR procedures relying on the standard reference methods LI, HE, TV and on the fourth-order variational methods CH and  $\text{TV-H}^{-1}$ .

|                    | Region 2 | Region 3 |
|--------------------|----------|----------|
| PA                 | 0.576    | 0.674    |
| LI                 | 0.915    | 0.873    |
| HE                 | 0.920    | 0.876    |
| TV                 | 0.678    | 0.825    |
| CH                 | 0.904    | 0.874    |
| $\text{TV-H}^{-1}$ | 0.968    | 0.891    |

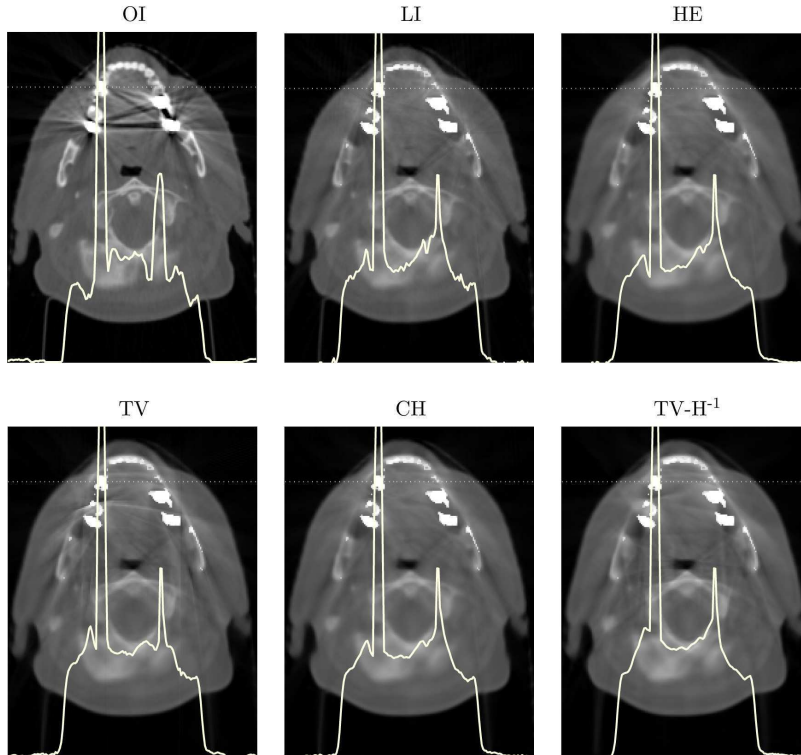


Figure 7: From left to right, from top to bottom, the original image containing metal artifacts (OI) and the corrected images of the MAR procedures relying on the LI, HE, TV, CH and  $\text{TV-H}^{-1}$  methods. White solid lines show the profile of the attenuation coefficient related to the probing line highlighted by the dashed white lines.

## 4 Discussion and Conclusion

A promising way to reduce artifacts caused by permanent metallic implants in CT images is provided by interpolation-based methods, which aim at identifying the corrupted parts of the sinogram and replacing them using information coming from the uncorrupted neighboring projections.

Fourth-order variational methods relying on the Chan-Hilliard equation and the  $\text{TV-H}^{-1}$  inpainting equation were profitably employed in other branches of image processing [16, 18, 19], but never used before to perform sinogram inpainting. These methods allow the connection of wide inpainting regions smoothly and can be solved with a fast solver.

Moving from these considerations, we have verified if the same methods can also be used to effectively restore those parts of the sinogram that are affected by metal artifacts, in order to perform MAR in CT scans.

With reference to the synthetic image, our analysis relies both on visual inspection and similarity indexes calculations, since original data free from metal

artifacts are known. In more detail, we have first compared the results of the methods under consideration in terms of the PSNR and the NCC indexes, evaluated on significant regions of the image (see Table 1 and Figure 3). The former was already applied to this kind of applications [13], while the latter was widely employed in other areas of medical image processing. Then, in order to test the capabilities of the two methods at hand in preserving and restoring structural informations, we have compared segmentations of small regions in the processed images (see Figure 5 and Figure 6). Comparisons have been made in terms of the DSC index (see Table 2). This is the most-widely used similarity measure in image segmentation analysis and it is our belief that it can represent a faithful indicator of the ability of a MAR method to recover hidden structures and to preserve morphological information, which are tasks of primary importance in the medical field. As far as we know, this is the first time that the DSC index has been applied in this context.

On the other hand, analysis developed on the real CT scan rely on visual inspections involving also the profile of the attenuation coefficient related to an explicative probing line as in [7, 22, 23].

Preservation and substantial improvement of the information content related to synthetic data is achieved by all the methods at the hand. In fact, they are able to reduce dark strikes due to metal artifacts and to enhance all the proposed similarity indexes. The worst results are obtained with the TV method, while the LI, HE and CH methods have comparable performances. The TV- $H^{-1}$  method outperforms the others providing highest similarity indexes, best image restoration and being the only one able to recover hidden structures (see Figure 4). This is also suggested by the results related to the clinical image (see Figure 7), where profile lines confirm the supremacy of TV- $H^{-1}$  method in correcting metal artifacts and restoring regions with uniform gray values.

The obtained results suggest that the HE and TV methods are less effective than the fourth-order variational methods at least to perform sinogram inpainting, as we could expect since they rely on second-order PDEs. The same results also support the idea that the CH method performs worse than the TV- $H^{-1}$  method, probably because it is conceived for high contrast or binary images, while here we are dealing with images characterized by large numbers of gray values. In conclusion, on the basis of the results here presented and the considerations drawn above, we support the use of the fourth-order variational method relying on the TV- $H^{-1}$  inpainting equation in sinogram restoration and metal artifact reduction. Future researches will aim at further investigating the performance of this method using additional CT scans of patients with metallic implants as well as at designing more accurate segmentation algorithms than the threshold method here used, in order to improve the performance of the present MAR procedure relying on the TV- $H^{-1}$  variational method. Finally, as an additional research perspective, we believe that the performance of our MAR procedure can be improved by adding a further step that combines the results of the TV- $H^{-1}$  inpainting together with the original sinogram data, namely through a procedure

as the ones proposed in [8, 24].

## Acknowledgment

The authors would like to thank prof. A. Bertozzi for her valuable suggestions which have helped us improving our paper.

## References

- [1] M. L. Kataoka, M. G. Hochman, E. K. Rodriguez, P.-J. P. Lin, S. Kubo, and V. D. Raptopoulos, “A review of factors that affect artifact from metallic hardware on multi-row detector computed tomography,” *Current problems in diagnostic radiology*, vol. 39, no. 4, pp. 125–136, 2010.
- [2] G. Wang, D. L. Snyder, J. O’Sullivan, and M. Vannier, “Iterative deblurring for ct metal artifact reduction,” *Medical Imaging, IEEE Transactions on*, vol. 15, no. 5, pp. 657–664, 1996.
- [3] D. D. Robertson, J. Yuan, G. Wang, and M. W. Vannier, “Total hip prosthesis metal-artifact suppression using iterative deblurring reconstruction,” *Journal of computer assisted tomography*, vol. 21, no. 2, pp. 293–298, 1997.
- [4] B. De Man, J. Nuyts, P. Dupont, G. Marchal, and P. Suetens, “Reduction of metal streak artifacts in x-ray computed tomography using a transmission maximum a posteriori algorithm,” in *Nuclear Science Symposium, 1999. Conference Record. 1999 IEEE*, vol. 2. IEEE, 1999, pp. 850–854.
- [5] J. Nuyts, B. De Man, P. Dupont, M. Defrise, P. Suetens, and L. Mortelmans, “Iterative reconstruction for helical ct: a simulation study,” *Physics in medicine and biology*, vol. 43, no. 4, p. 729, 1999.
- [6] W. A. Kalender, R. Hebel, and J. Ebersberger, “Reduction of ct artifacts caused by metallic implants.” *Radiology*, vol. 164, no. 2, pp. 576–577, 1987.
- [7] E. Meyer, F. Bergner, R. Raupach, T. Flohr, and M. Kachelrieß, “Normalized metal artifact reduction (nmar) in computed tomography,” in *Nuclear Science Symposium Conference Record (NSS/MIC), 2009 IEEE*. IEEE, 2009, pp. 3251–3255.
- [8] E. Meyer, R. Raupach, B. Schmidt, A. H. Mahnken, and M. Kachelrieß, “Adaptive normalized metal artifact reduction (anmar) in computed tomography,” in *Nuclear Science Symposium and Medical Imaging Conference (NSS/MIC), 2011 IEEE*. IEEE, 2011, pp. 2560–2565.
- [9] M. Bazalova, L. Beaulieu, S. Palefsky, and F. Verhaegen, “Correction of ct artifacts and its influence on monte carlo dose calculations,” *Medical physics*, vol. 34, p. 2119, 2007.

- [10] M. Abdoli, M. R. Ay, A. Ahmadian, and H. Zaidi, “Reduction of dental filling metallic artifacts in ct-based attenuation correction of pet data using weighted virtual sinograms,” in *Nuclear Science Symposium Conference Record (NSS/MIC), 2009 IEEE*. IEEE, 2009, pp. 2752–2755.
- [11] S. Zhao, D. Robeltson, G. Wang, B. Whiting, and K. T. Bae, “X-ray ct metal artifact reduction using wavelets: an application for imaging total hip prostheses,” *Medical Imaging, IEEE Transactions on*, vol. 19, no. 12, pp. 1238–1247, 2000.
- [12] X. Duan, L. Zhang, Y. Xiao, J. Cheng, Z. Chen, and Y. Xing, “Metal artifact reduction in ct images by sinogram tv inpainting,” in *Nuclear Science Symposium Conference Record, 2008. NSS’08. IEEE*. IEEE, 2008, pp. 4175–4177.
- [13] Y. Zhang, Y.-F. Pu, J.-R. Hu, Y. Liu, Q.-L. Chen, and J.-L. Zhou, “Efficient ct metal artifact reduction based on fractional-order curvature diffusion,” *Computational and mathematical methods in medicine*, vol. 2011, 2011.
- [14] J. Shen and T. F. Chan, “Mathematical models for local nontexture inpaintings,” *SIAM Journal on Applied Mathematics*, vol. 62, no. 3, pp. 1019–1043, 2002.
- [15] J. Shen, S. H. Kang, and T. F. Chan, “Euler’s elastica and curvature-based inpainting,” *SIAM Journal on Applied Mathematics*, vol. 63, no. 2, pp. 564–592, 2003.
- [16] A. L. Bertozzi, S. Esedoglu, and A. Gillette, “Inpainting of binary images using the cahn–hilliard equation,” *Image Processing, IEEE Transactions on*, vol. 16, no. 1, pp. 285–291, 2007.
- [17] A. Bertozzi, S. Esedoglu, and A. Gillette, “Analysis of a two-scale cahn–hilliard model for binary image inpainting,” *Multiscale Modeling & Simulation*, vol. 6, no. 3, pp. 913–936, 2007.
- [18] M. Burger, L. He, and C.-B. Schönlieb, “Cahn–hilliard inpainting and a generalization for grayvalue images,” *SIAM Journal on Imaging Sciences*, vol. 2, no. 4, pp. 1129–1167, 2009.
- [19] C.-B. Schönlieb, A. Bertozzi, M. Burger, L. He *et al.*, “Image inpainting using a fourth-order total variation flow,” 2009.
- [20] C.-b. Schönlieb and A. Bertozzi, “Unconditionally stable schemes for higher order inpainting,” *Communications in Mathematical Sciences*, vol. 9, no. 2, pp. 413–457, 2011.
- [21] L. Dice, “Measures of the amount of ecologic association between species,” *Ecology*, vol. 26, no. 3, pp. 297–302, 1945.

- [22] Y. Chen, Y. Li, H. Guo, Y. Hu, L. Luo, X. Yin, J. Gu, and C. Toumoulin, “Ct metal artifact reduction method based on improved image segmentation and sinogram in-painting,” *Mathematical Problems in Engineering*, vol. 2012, 2012.
- [23] A. Amirkhanov, M. Reiter, J. Kastner, M. E. Gröller, and C. Heinzl, “Evaluation of projection-based metal-artifact reduction for multi-material components.”
- [24] E. Meyer, R. Raupach, M. Lell, B. Schmidt, and M. Kachelrieß, “Frequency split metal artifact reduction (fsmar) in computed tomography,” *Medical physics*, vol. 39, pp. 1904–1916, 2012.

# MOX Technical Reports, last issues

Dipartimento di Matematica “F. Brioschi”,  
Politecnico di Milano, Via Bonardi 9 - 20133 Milano (Italy)

- 15/2013** ANTONIETTI, P.F.; GIANI, S.; HOUSTON, P.  
*Domain Decomposition Preconditioners for Discontinuous Galerkin Methods for Elliptic Problems on Complicated Domains*
- 16/2013** FAGGIANO, E. ; LORENZI, T. ; QUARTERONI, A.  
*Metal Artifact Reduction in Computed Tomography Images by Variational Inpainting Methods*
- 14/2013** GIANNI ARIOLI, FILIPPO GAZZOLA  
*A new mathematical explanation of the Tacoma Narrows Bridge collapse*
- 13/2013** PINI, A.; VANTINI, S.  
*The Interval Testing Procedure: Inference for Functional Data Controlling the Family Wise Error Rate on Intervals.*
- 12/2013** ANTONIETTI, P.F.; BEIRAO DA VEIGA, L.; BIGONI, N.; VERANI, M.  
*Mimetic finite differences for nonlinear and control problems*
- 11/2013** DISCACCIATI, M.; GERVASIO, P.; QUARTERONI, A.  
*The Interface Control Domain Decomposition (ICDD) Method for Elliptic Problems*
- 10/2013** ANTONIETTI, P.F.; BEIRAO DA VEIGA, L.; MORA, D.; VERANI, M.  
*A stream virtual element formulation of the Stokes problem on polygonal meshes*
- 09/2013** VERGARA, C.; PALAMARA, S.; CATANZARITI, D.; PANGRAZZI, C.; NOBILE, F.; CENTONZE, M.; FAGGIANO, E.; MAINES, M.; QUARTERONI, A.; VERGARA, G.  
*Patient-specific computational generation of the Purkinje network driven by clinical measurements*
- 08/2013** CHEN, P.; QUARTERONI, A.; ROZZA, G.  
*A Weighted Reduced Basis Method for Elliptic Partial Differential Equations with Random Input Data*

**07/2013** CHEN, P.; QUARTERONI, A.; ROZZA, G.  
*A Weighted Empirical Interpolation Method: A-priori Convergence Analysis and Applications*